Structural Aspects of the Attached Turbulent Boundary Layer Flow Over a Hill

Julie E Duetsch-Patel (✉ juliedp@vt.edu)

Virginia Tech

Aldo Gargiulo

Virginia Tech

Aurelien Borgoltz

Virginia Tech

William J Devenport

Virginia Tech

K Todd Lowe

Virginia Tech

001
002
003
004
005
006
007
008
009
010

Structural Aspects of the Attached Turbulent Boundary Layer Flow Over a Hill

Julie E. Duetsch-Patel[1*], Aldo Gargiulo[1†], Aurelien Borgoltz[1†], William J. Devenport[1†] and K. Todd Lowe[1*†]

[1*]Kevin T. Crofton Department of Aerospace and Ocean Engineering, Virginia Tech, 460 Old Turner St, Blacksburg, 24061, VA, USA.

*Corresponding author(s). E-mail(s): juliedp@vt.edu; kelowe@vt.edu;
Contributing authors: galdo@vt.edu; aborgolt@vt.edu; devenport@vt.edu;
[†]These authors contributed equally to this work.

Abstract

Three-dimensional turbulent boundary layers under strong pressure gradients and curvature are the rule in real-world flow applications but are typically not well predicted by turbulence models due to isotropic eddy viscosity or equilibrium assumptions. Validation-quality data in complex 3D flows is necessary for continued efforts to improve simulation accuracy. The BeVERLI (**Be**nchmark **V**alidation **E**xperiments for **R**ANS/**L**ES **I**nvestigations) Hill bump model, designed specifically for validation experiments, was tested in the Virginia Tech Stability Wind Tunnel to collect validation experiment data on the three-dimensional (3D) boundary layer flow over a 3D hill. Laser Doppler velocimetry measurements on the bump model were used to study the mean flow and turbulence structure and evaluate the impact of pressure gradient and curvature upon the total shear stress in the boundary layer and evaluate the impact of pressure gradient and curvature upon the total shear stress behavior in the near-wall region. From analysis of the BeVERLI Hill flow, including the boundary layer just upstream of the hill, and comparison with the 3D flow around a wing-body junction of Ölçmen et al (2001), it is shown that none of the stations studied exhibit a constant shear stress region over any significant region of the boundary layer. One station on the hill, located in a region

011
012
013
014
015
016
017
018
019
020
021
022
023
024
025
026
027
028
029
030
031
032
033
034
035
036
037
038
039
040
041
042
043
044
045
046

with strong spanwise and streamwise pressure gradients, experiences an apparent return to an equilibrium shear stress for $x_2^+ < 30$ due to significantly increased production of $\overline{u_1'u_2'}$ and $\overline{u_2'^2}$ at this station.

1 Introduction

Three-dimensional turbulent boundary layers (3D TBLs) are of extensive interest for practical engineering applications, but have been less frequently studied than two-dimensional turbulent boundary layers (2D TBLs). Due to the challenges that three-dimensional boundary layers present to accurate computational modeling, their continued study is relevant today. Some well-known features of 3DTBLs include the lag between the shear-stress direction vector and the velocity-gradient vector direction, a reduction in near-wall turbulent kinetic energy and Reynolds stresses, and a reduction in the turbulence parameter A_1 below its typical 2D value of 0.15, to as low as 0.03 to 0.05 in the case of Anderson and Eaton (1989). Because of this, 3D TBLs present a particular challenge to modeling, as the stress/strain misalignment invalidates the assumptions behind any turbulence models that assume an isotropic eddy viscosity. This limits the utility of some popular Reynolds-Averaged Navier Stokes (RANS) computational fluid dynamics (CFD) turbulence models for flows of engineering interest, even as CFD is increasingly used for high-impact decisions in vehicle design. Improved modeling of 3D flows depends upon a better understanding of 3D boundary layers and turbulence to improve the assumptions that go into turbulence models.

Unlike RANS, large-eddy simulation (LES) resolves the larger turbulence scales and models the small scales that cannot be resolved on the grid. As a result, LES requires a sub-grid scale (SGS) model for the effects of the small scales on the resolved flow. Per Bose and Park (2018), the total number of grid points required for wall-resolved and wall-modeled LES are $N_{WR} \approx Re_L^{13/7}$ and $N_{WM} \approx Re_L$, respectively. Because of this, wall-resolved LES is infeasible for higher Reynolds number applications, requiring wall-modeled LES. Like RANS turbulence models, existing wall models are largely built on equilibrium assumptions, which are not valid in the vast majority of applicable 3D flows. These assumptions can be built into the model directly, for example through assuming an equilibrium stress or velocity distribution, or indirectly through assumptions regarding eddy viscosity and inner-layer Reynolds stress (Bose and Park, 2018).

Equilibrium two-dimensional boundary layers typically have a region near the wall where the total shear stress is nearly constant, approximately $0.95 \leq \tau_{total}/\tau_w \leq 1$ for sufficiently high Reynolds numbers. Devenport and Lowe (2022) demonstrate the derivation of 2D zero-pressure gradient boundary

layer equations that produce this behavior, showing that as the viscous shear stress decreases rapidly outside the viscous sublayer, the turbulent shear stress increases to balance out the total shear stress. In non-zero pressure gradient flows, a linear gradient of the total shear stress will be present instead.

Equilibrium approximations to the thin-boundary layer equations are often made to relax strict assumptions on the velocity profile that would otherwise be required for LES (Bose and Park, 2018). These approximations also lead to the assumption of a constant total stress region in the near-wall region of the boundary layer. However, most flows of engineering interest involve strong pressure gradients in both the streamwise and lateral direction and other non-equilibrium phenomena, which will invalidate these assumptions.

The flow over a wall-mounted bump is a common test case to the goal of improved computational fidelity (e.g. Byun and Simpson (2006); Bell et al (2012)), as the simple geometry generates a flow field with pressure gradient, curvature effects, and three-dimensional boundary layer separation and reattachment. All these features are generally challenging for CFD and are very common in practical applications. This work presents results from experiments studying the three-dimensional turbulent attached and separated flow over the BeVERLI (**Be**nchmark **V**alidation **E**xperiment for **R**ANS/**L**ES **I**nvestigations) Hill. The flow over this model experiences three-dimensional pressure gradients of varying sign and magnitude, skewing, three-dimensional curvature, and three-dimensional flow effects. We study the evolution of the boundary layer from upstream of the hill to over the hill itself, specifically the impact of curvature, 3D pressure gradients, and skewing upon the total shear stress distribution in the boundary layer. Results are also compared RANS simulations and with the 3D TBL flow over a flat wall around a wing-body junction of Ölçmen et al (2001), which also experiences three-dimensional pressure gradients and flow skewing. It will be shown that streamwise and lateral pressure gradients and skewing significantly impact the flow, reducing the turbulent shear stress throughout the boundary layer and resulting in no constant shear stress region for any of the stations studied. Any model that relies on equilibrium shear stress assumptions will not be able to accurately predict turbulence in three-dimensional turbulent boundary layers.

2 Methodology

2.1 Stability Wind Tunnel

Experiments were conducted in the Stability Wind Tunnel (SWT) at Virginia Tech, a continuous, single-return subsonic wind tunnel, with a 1.85 x 1.85 x 7.32 m test section. A schematic of the facility is shown in Fig. 1. The SWT is capable of reaching a maximum flow speed of approximately 80 m/s, corresponding to a Reynolds number per meter of 5×10^6. The facility features two interchangeable test sections, one of which has highly modular side walls to facilitate model and instrumentation installation (Duetsch-Patel et al, 2020), as well as an instrumented contraction liner to track the surface static pressure

through the contraction (Vishwanathan et al, 2020). Measurements over the BeVERLI Hill were performed in a configuration as depicted in Fig. 2.
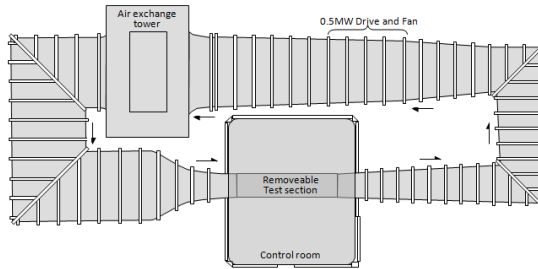

Fig. 1: Virginia Tech Stability Wind Tunnel

Extensive characterization has been conducted for the facility, including measurements of boundary layer and cross-sectional flow variations. An example of this characterization is measurements of the inflow boundary layer made using a 32-probe boundary layer rake. Measurements obtained for two different experimental builds in February 2020 and May 2021 were shown to be in good agreement. The inflow boundary layer profile at three points across the span of the inflow is shown in Fig. 3, and the inflow boundary layer parameters are shown in Table 1.
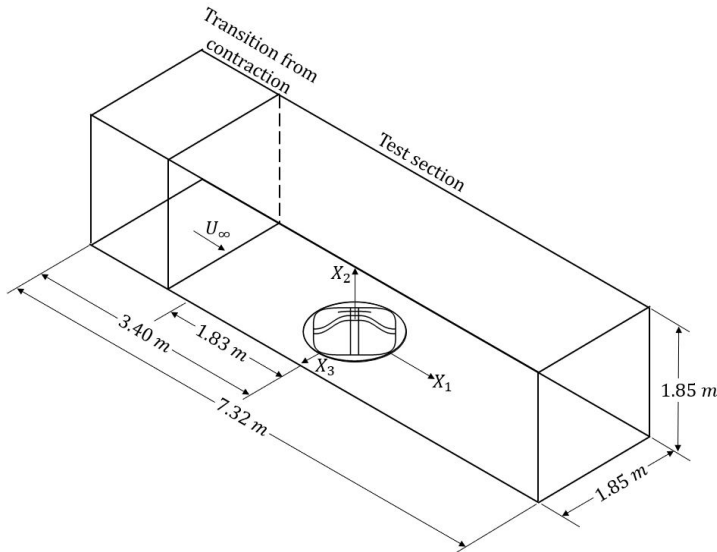

Fig. 2: The SWT test section and bump configuration. The side wall is shown as the floor to accurately portray the right-handed coordinate system.
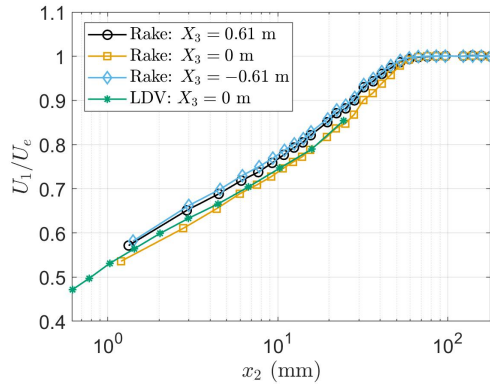
Fig. 3: Inflow boundary layer profile of the Stability Wind Tunnel inflow at $Re_H = 250,000$.

Table 1: Inflow boundary layer parameters across the span of the inflow to the SWT test section, where $Re_\theta = U_\infty \theta / \nu$ and $Re_\tau = u_\tau \delta_{99}/\nu$, with u_τ computed via Spalding fit to the boundary layer profile.

X_3 (m)	δ_{99} (mm)	δ^* (mm)	θ (mm)	Re_θ	Re_τ
0.61	55.0	7.3	5.5	7382	2764
0	57.2	8.7	6.5	8686	2793
-0.61	51.8	7.0	5.3	7132	2629

2.2 BeVERLI Hill Model

The bump geometry is defined in detail by Gargiulo et al (2020) and has a design length of 0.93472 m and a height of 0.1869 m. The 2D centerline and centerspan cross-section of the 3D geometry is defined by a fifth-degree polynomial mirrored about $x_1 = 0$, with a flat top region in the center connecting the two polynomials to form a cruciform. These profiles form cylindrical regions 0.0935 m wide. The edges of these perpendicular cylindrical sections are connected at a constant height using a fourth order superellipse. Because of these features, the model exhibits 90 degree rotational symmetry, allowing for different orientations of the model with respect to the incoming flow. For these experiments, the bump was oriented as shown in Fig. 2 with one of the pairs of rounded corners directly aligned with the approaching freestream. This orientation is referred to as the 45° yaw case. Coordinate systems labeled X_i indicate global coordinates, with the origin at the center of the hill as shown in Fig. 2, while coordinate systems labeled lowercase x_i indicate local wall-shear stress coordinates, with the origin at the wall-location of the profile. The hill was mounted on the wind tunnel side wall to facilitate access to embedded instrumentation.

231 Two CNC-milled models were used: One with 135 pressure taps installed
232 in the surface and one with slots for clear windows for laser Doppler velocime-
233 try (LDV) measurements along the fifth-degree polynomial curves. The models
234 were scanned after manufacturing but before paint was applied to the surface
235 with a GOM ATOS 5 blue light laser scanner with a resolution of 8 mexapix-
236 els. These scans found that the manufactured geometry matched the design
237 geometry to within ± 0.40 mm and ± 0.30 mm, respectively.

238 The hill was installed 6.88 m downstream of the 3.18 mm boundary layer
239 trip in the wind tunnel contraction, and 1.83 m downstream of the inflow to
240 the test section. Measurements were made with the freestream flow adjusted to
241 ensure height-based Reynolds numbers Re_H of $250,000 \pm 5000$, $325,000 \pm 5000$,
242 and $650,000 \pm 5000$. Measurements collected at $Re_H = 250,000$ are the focus
243 of this study.

2.3 Instrumentation

247 Pressure measurements on the model surface were collected using 1.6 mm
248 (0.063 in) diameter embedded steel tubes, which were connected via tub-
249 ing to pressure scanners. Ninety-five taps were connected to three DTC ESP
250 32 HD scanners with a range of 2.5 psi and a manufacturer-rated accu-
251 racy of 0.06% full-scale. The remaining taps were connected to an Esterline
252 9816/98RK pressure scanner with a rated accuracy of 0.05% full scale. Com-
253 prehensive uncertainty estimations in the style of Aeschliman and Oberkampf
254 (1998) and Rhode and Oberkampf (2017) found an uncertainty in static pres-
255 sure coefficient measurements on the bump, including random uncertainty,
256 flowfield nonuniformity uncertainty, and instrumentation and model geometry
257 uncertainty, to be ± 0.025 at $Re_H = 250,000$ at 95% confidence.

258 A specialized embedded three-component LDV system was used to take
259 measurements of the turbulent boundary layer over the bump surface and
260 upstream of the model. The probe was mounted inside the bump, with five
261 laser beams passing through the 1.5mm anti-reflective curvature-fitting acrylic
262 windows, as shown in Fig. 4. Three beams are generated with a continuous
263 wave, frequency-doubled, diode pumped ND:YVO4 solid state Coherent Verdi
264 V6 laser with a wavelength of 532 nm, while two beams are generated with a
265 continuous wave, single-line mode, optically pumped semiconductor Coherent
266 Genesis MX laser with a wavelength of 488 nm.

267 Three measurement volumes were created from the intersection of the
268 five beams to obtain three components of velocity. IntraAction Corporation
269 acousto-optic modulators were used to frequency shift one beam out of each
270 pair forming a measurement volume to generate a moving interference fringe
271 pattern. This moving fringe pattern recovers directional information on the
272 movement of the particle through the measurement volume that would be lost
273 if a static fringe pattern were used. Two of the three green Verdi V6 beams
274 were frequency-shifted by +40 MHz and -80 MHz, respectively, while one of
275 the two Genesis MX beams was frequency-shifted by +60 MHz. The Verdi V6
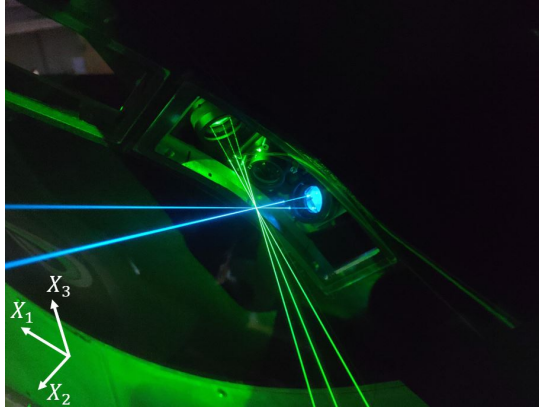276 was operated at approximately 0.8-1.2 W and the Genesis MX was operated

Fig. 4: The LDV probe embedded in the BeVERLI hill while collecting data at Station W3. The five beams used in this system are split between two probe heads. The probe head in the center contains receiving optics.
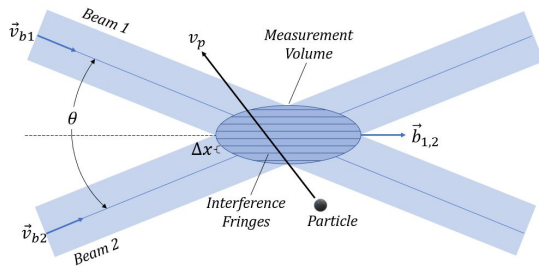

Fig. 5: Intersection of two beams to form one measurement volume, measuring one component of velocity. Δx indicates the spacing between interference fringes generated by the intersection, and $\overrightarrow{b}_{1,2}$ is the bisector of the beam direction vectors, $\overrightarrow{v}_{b1}$ and $\overrightarrow{v}_{b2}$.

at approximately 0.25 to 0.50 W during testing. The laser beam power emitted from the probe was approximately 70-100 mW after passing through table optics and fibers.

Velocity components are measured perpendicular to the local interference fringes generated by the intersection of a given pair of laser beams, as shown in Fig. 5. Each component is a function of the detected Doppler frequency (f_D) generated by the light scattered by the particle as it passes through the fringes and the fringe spacing (Δx), as shown in Eq. 1. The spacing of interference fringes created by the intersection of two laser beams is a function of the beam wavelength (λ_b) and the angle between the beams (θ).

$$v_{p_i} = f_{D_i} \Delta x_i = f_{D_i} \frac{\lambda_{b_i}}{2 \sin{(\theta/2)_i}} \tag{1}$$

277
278
279
280
281
282
283
284
285
286
287
288
289
290
291
292
293
294
295
296
297
298
299
300
301
302
303
304
305
306
307
308
309
310
311
312
313
314
315
316
317
318
319
320
321
322

323   These velocity components are in a non-orthogonal coordinate system due
324   to the non-orthogonal orientation of the fringe and measurement volume inter-
325   sections, and thus must be converted to orthogonal coordinates. The vector
326   in the fringe-perpendicular direction can be computed by measuring the beam
327   direction vectors, $\overrightarrow{v}_{b1}$ and $\overrightarrow{v}_{b2}$ for a given pair. From the view of Fig. 5,
328   the cross-product of these two vectors will yield a vector pointing out of the
329   page. The cross-product of this vector with the bisector of $\overrightarrow{v}_{b1}$ and $\overrightarrow{v}_{b2}$,
330   $\overrightarrow{b}_{1,2}$, results in a vector perpendicular to the fringe direction. The specific
331   direction of the vector (pointing towards the top of the page or bottom of
332   the page in Fig. 5) depends on the sign of the frequency shift that generates
333   the moving fringe pattern. This transformation can be completed for each of
334   the three measurement volumes, resulting in the transformation between the
335   non-orthogonal, fringe-perpendicular velocity components, C_i, and orthogonal
336   tunnel velocity components, U_i, as shown in Eq. 2. Here, $\overrightarrow{d}_{g,N}$ is laser beam
337   direction for the green Verdi V6 laser for N frequency shift (0 for unshifted,
338   40 for +40 MHz, and 80 for -80 MHz), $\overrightarrow{d}_{b,N}$ is laser beam direction for the
339   blue Genesis MX laser for N frequency shift (0 for unshifted and 60 for +60
340   MHz), and $\overrightarrow{b}_{0,N}$ is the vector bisecting the two laser beam directions. The
341   components in the second row are negated due to the negative frequency shift
342   for this component. Extracting the orthogonal velocity components requires
343   the inverse transformation matrix to be calculated.

$$\begin{bmatrix} C_1 \\ C_2 \\ C_3 \end{bmatrix} = \begin{bmatrix} (\overrightarrow{v}_{g,0} \times \overrightarrow{v}_{g,40}) \times \overrightarrow{b}_{0,40} \\ -(\overrightarrow{v}_{g,0} \times \overrightarrow{v}_{g,80}) \times \overrightarrow{b}_{0,80} \\ (\overrightarrow{v}_{b,0} \times \overrightarrow{v}_{b,60}) \times \overrightarrow{b}_{0,60} \end{bmatrix} \begin{bmatrix} U_1 \\ U_2 \\ U_3 \end{bmatrix} = \begin{bmatrix} t_{11} & t_{12} & t_{13} \\ t_{21} & t_{22} & t_{23} \\ t_{31} & t_{32} & t_{33} \end{bmatrix} \begin{bmatrix} U_1 \\ U_2 \\ U_3 \end{bmatrix} \quad (2)$$

351   Once the data is in tunnel coordinates, an additional transformation into
352   wall-shear stress coordinates is completed via successive rotation matrices
353   applied to the data, as shown in Eq. 3. First, the coordinates are rotated by the
354   hill yaw angle (θ_{x_2} for this study) to rotate the data into the plane of the cylin-
355   drical hill windows. A rotation about the new x_3-axis by the local wall-normal
356   angle converts the data into coordinates normal to the local surface curvature.
357   A final rotation about this surface-normal x_2-axis by $\theta_W = \arctan(U_3/U_1)_w$
358   at the nearest-wall profile point converts the data into local wall-shear stress
359   coordinates.

$$R_W = \begin{bmatrix} \cos(\theta_W) & 0 & \sin(\theta_W) \\ 0 & 1 & 0 \\ -\sin(\theta_W) & 0 & \cos(\theta_W) \end{bmatrix} \begin{bmatrix} \cos(\theta_N) & \sin(\theta_N) & 0 \\ -\sin(\theta_N) & \cos(\theta_N) & 0 \\ 0 & 0 & 1 \end{bmatrix} \begin{bmatrix} \cos(\theta_{x_2}) & 0 & -\sin(\theta_{x_2}) \\ 0 & 1 & 0 \\ \sin(\theta_{x_2}) & 0 & \cos(\theta_{x_2}) \end{bmatrix}$$
$$(3)$$

366   The Doppler frequency signals are obtained using AURStudio from AUR,
367   Inc, which uses Fourier domain processing for Doppler frequency estimates
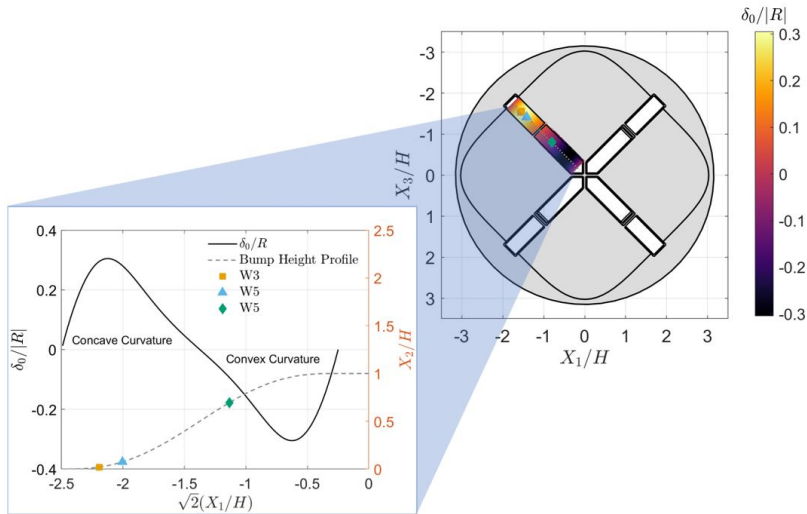368   from photodetector signals. One block of samples (ranging from 5,000 to 15,000

Fig. 6: The ratio of inflow boundary layer thickness on the tunnel centerline, δ_0, to the local magnitude of the 3D radius of curvature, R. $\delta_0/R > 0$ indicates concave curvature, while $\delta_0/R < 0$ indicates convex curvature. Symbols show the location of the hill stations on the local surface curvature.

samples) was taken at each measurement point above the wall. Near-wall points were collected over approximately one minute of sampling time to prevent seed particles from collecting on the acrylic windows, and thus typically had fewer samples than points taken above $x_2 \approx 0.5$ mm. Data further above the surface was collected over approximately one to three minutes of sampling time. During post-processing, outlying points from histograms were removed. Nominal x_2-heights at each point in the profile were corrected by fitting the nearest-wall data to $U_1^+ = x_2^+$ for data in the linear sublayer. The measurement volume was approximately 45 μm in diameter, and measurements were achievable at a minimum and maximum height above the wall of 0.1 mm and 30 mm, respectively. The flow was seeded using a mineral oil smoke machine (MDG MAX 3000 APS) with particles ranging in size from 0.5 to 1 μm, resulting in Stokes numbers small enough to capture the full range of relevant scales.

Data was collected at 13 locations on the bump surface, as well as at the inflow to the test section and on the flat wall just upstream of the hill. For this study, four locations on and upstream of the hill are of interest at $Re_H = 250,000$, as shown in Table 2. These specific stations were chosen for this analysis because they are all in attached flow regions and have at least one point in the profile that is in or very near the edge of the linear sublayer, allowing for a direct calculation of τ_w from the velocity gradient. The ratio of the centerline inflow boundary layer thickness to radius of curvature magnitude at the stations of interest on the hill is shown in Fig. 6.

Table 2: LDV data locations of interest for this study, focusing on Windward (W) stations. γ_{FA} is the mean flow angle closest to the wall relative to the global x_1 axis, δ_0/R is the ratio of the empty tunnel boundary layer thickness at the location of the bump height to the local radius of curvature at each station, and $\beta_{X_i} = (\delta^*_{inflow}/\tau_{w,inflow})(\partial P/\partial X_i)$ is the Clauser parameter.

Station	Symbol	X_1/H	X_2/H	X_3/H	u_τ/U_∞	Min x_2^+	Max x_2^+	γ_{FA} (°)	δ_0/R	β_{X_1}	β_{X_3}
W1	●	-4.1	0	0	0.035	5.8	721	0	0	1.3	0
W2	▲	-1.55	0.02	-1.55	0.037	5.3	1139	-38.9	0.38	-3.1	0.9
W3	▪	-1.42	0.07	-1.42	0.038	2.0	1202	-37.4	0.36	-1.7	2.4
W5	◆	-0.80	0.70	-0.80	0.043	4.3	898	16.0	-0.12	-4.4	5.4

Rigorous uncertainty quantification encompassing many uncertainty sources (e.g. article geometry uncertainty effects and repeatability of measurements) is critical for the BeVERLI Hill experiments to ensure the results are suitable for CFD validation. Comprehensive uncertainty quantification has been conducted on the LDV measurements, encompassing uncertainty from instrumentation sources including statistical convergence, signal processor resolution, precision in beam alignment, laser coherence, and the precision of the rotation matrix to transform the data from the non-orthogonal probe coordinates to an orthogonal coordinate system. In addition, the Error Sampling Method of Smith and Oberkampf (2014) has been applied to the data, comparing results across repeated runs to isolate sources due to uncertainty in the linear traverse motion and variations in flow conditions between runs.

The uncertainty components of these two sources (instrumentation error, dominated by bias error sources, and error sampling, dominated by random error sources) have been combined via a root-sum square to arrive at the total uncertainty interval for the mean velocities and turbulence components in global tunnel coordinates. For data given in wall-shear stress coordinates, the additional uncertainty due to the additional coordinate system transformations have also been incorporated into the results, resulting in comprehensive uncertainty estimates for the mean velocities and Reynolds stresses. Uncertainties for derived components, such as shear stress and turbulence production components, was completed via propagation of uncertainties.

Each profile has its own set of uncertainties at each point given the specific setup and conditions for that profile, and, as such, error bars are shown for each dataset and are of different magnitudes at different stations. Representative 95% confidence uncertainties are given in Table 3.

Table 3: Representative 95% confidence uncertainties of LDV mean velocities and Reynolds stresses.

Term	Uncertainty
U_1/U_∞	0.029
U_2/U_∞	0.023
U_3/U_∞	0.072
$\overline{u_1'^2}/U_\infty^2$	0.00091
$\overline{u_2'^2}/U_\infty^2$	0.00070
$\overline{u_3'^2}/U_\infty^2$	0.00085
$\overline{u_1'u_2'}/U_\infty^2$	0.00039
$\overline{u_1'u_3'}/U_\infty^2$	0.00087
$\overline{u_2'u_3'}/U_\infty^2$	0.00045

3 Results

Laser Doppler velocimetry data at the four stations of interest are supplemented by surface static pressure contours, oil flow visualization, and RANS

507 CFD simulation results to analyze the global flowfield and the boundary layer
508 history leading up to stations W2, W3, and W5. In addition, experimental
509 data from the three-dimensional turbulent boundary layer flow on the flat
510 wall around a wing-body junction of Ölçmen et al (2001) is compared with
511 the experimental data on the BeVERLI hill under similar skewing conditions.
512 Pressure gradient and flow history effects are of primary focus, while effects of
513 the hill curvature will be studied in future work.

3.1 Pressure Distribution and Global Flowfield

517 Fig. 7a shows the mean freestream pressure coefficient contours over the entire
518 hill at $Re_H = 250,000$. As shown, the pressure gradient changes sign multiple
519 times over the surface in both the streamwise and spanwise directions as the
520 flow away from the centerline is accelerated around the sides of the model.
521 These strong streamwise and spanwise pressure gradients and 3D curvature
522 induce strong near-wall crossflow. LDV profile locations are indicated by the
523 black circles. The four stations of interest for this study are labeled. Fig. 7b
524 shows a focus view of the stations of interest on the hill, including wall-shear
525 stress direction (from the mean flow angle) indicated by black vectors, and the
526 mean flow direction $x_2^+ \approx 500$ indicated by blue vectors. The maximum x_2^+
527 captured at each profile is given in Table 2.
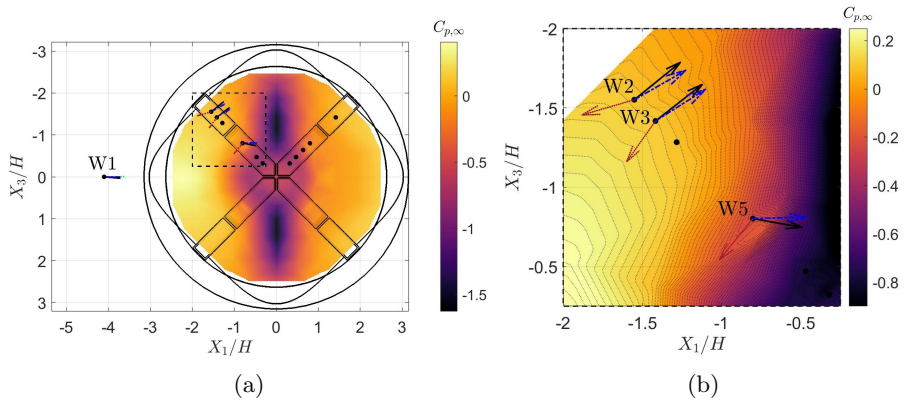

(a)   (b)

Fig. 7: Freestream pressure coefficient contours over the hill surface at $Re_H = 250,000$ in global coordinates. Black circles show LDV profile locations. Solid arrows indicate mean flow direction in the linear sublayer, dashed vectors indicate mean flow direction at $x_2^+ \approx 500$, and dotted vectors indicate the resultant direction of $\overrightarrow{\beta}$. (a) Full pressure coefficient contour on the hill surface. (b) Focus view of the three stations of interest on the bump. Here the pressure coefficient color range is limited to better show the surface pressure variations in this region.

The flow begins largely two-dimensional in an adverse pressure gradient (APG) at station W1 of $\beta = 1.3$. As the flow approaches the hill, the APG increases in strength up to the stagnation region on the front of the model, after which it is accelerated over the windward face of the hill. Along the sides, stations W2 and W3 experience similar pressure gradients and pressure gradient histories. At these stations, the flow direction next to the wall is skewed nearly 40° relative to the upstream flow direction, indicating strong deformation under the lateral pressure gradients present upstream of these stations. At W2, the direction of $\overrightarrow{\beta} = (\beta_{X_1}, 0, \beta_{X_3})$ is only just slightly angled off the horizontal axis, indicating that the streamwise pressure gradient effects should dominate at this location. The spanwise pressure gradient impact becomes much more significant at W3, as $\overrightarrow{\beta}$ tilts significantly in the positive X_3-direction as the spanwise pressure gradient begins to dominate.

In contrast, station W5 experiences an entirely different pressure gradient and pressure gradient history. The local streamwise pressure gradient remains favorable, as the near-wall flow direction remains nearly perpendicular to the local pressure coefficient contours. However, the lateral pressure gradients have induced milder skewing, pointing in the opposite direction relative to the skewing at W2 and W3. Here, the flow direction next to the wall is yawed 16° relative to the upstream flow direction and $\overrightarrow{\beta}$ indicates that the streamwise and spanwise pressure gradients are of a similar magnitude, although the spanwise component continues to dominate. The magnitudes of β_{X_1} and β_{X_3} are also the largest at this station at -4.4 and 5.4, respectively.

The surface static pressure coefficent contour at $Re_H = 250,000$ is shown overlaid with oil flow visualization images at $Re_H = 250,000$ and $Re_H = 650,000$ in Fig. 8. In the oil flow visualization images, gravity effects due to the hill's position on the side wall of the facility can be seen, especially in the lower Reynolds number case, when compared with the streamlines predicted by RANS CFD on the windward face of the hill. At $Re_H = 250,00$, the separated flow in the wake was not strong enough to prevent the oil mixture from flowing towards the floor under gravity (with the gravity vector pointing in the $-X_3$ direction). This also likely affected the windward side of the bump as well, as the windward streamlines are noticeably tilted more strongly in the direction of the floor than the streamlines at $Re_H = 650,000$ and in the CFD.

The effect of gravity on the oil flow visualization is supported by the similarity of the mean flow direction in the sublayer at stations W2 and W3 to the streamlines predicted by CFD at $Re_H = 650,000$. The discrepancy at W5 between the CFD and experiment could be due to the particular importance of flow history at this station. As shown in Fig. 7, the local pressure gradient at W5 is rapidly changing as the flow is accelerated around the side of the hill, and the near-wall flow has passed through the strong adverse pressure gradient and stagnation region near the windward foot of the hill. Given the strong variations and sign changes in pressure gradient that the flow will have experienced as it passed over the windward face of the bump and towards station W5, small differences between this pressure gradient and flow history
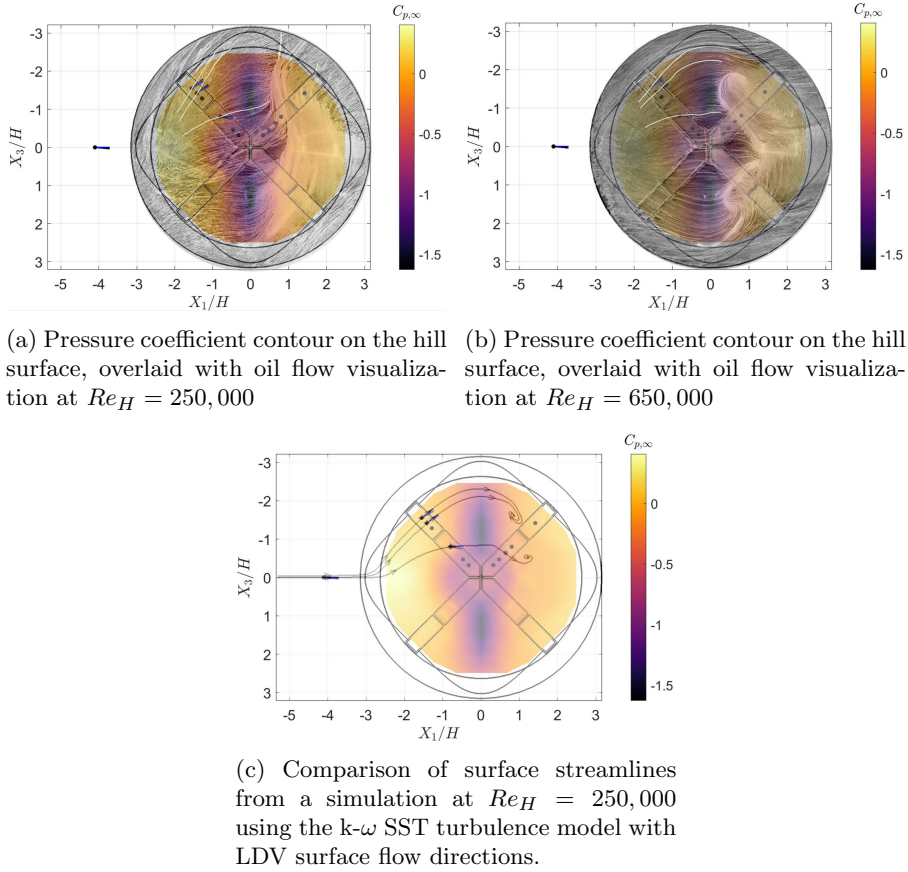
(a) Pressure coefficient contour on the hill surface, overlaid with oil flow visualization at $Re_H = 250,000$

(b) Pressure coefficient contour on the hill surface, overlaid with oil flow visualization at $Re_H = 650,000$

(c) Comparison of surface streamlines from a simulation at $Re_H = 250,000$ using the k-ω SST turbulence model with LDV surface flow directions.

Fig. 8: Freestream pressure coefficient distribution at $Re_H = 250,000$, overlaid with (a) oil flow visualization at $Re_H = 250,000$, (b) oil flow visualization at $Re_H = 650,000$, and (c) RANS simulation streamlines computed using the S-A turbulence model at $Re_H = 650,000$. In (a) and (b), additional white streamlines are drawn, tracing the path of the oil on the surface through the LDV stations W2, W3, and W5. The gravity vector in is in the $-X_3$ direction.

between LDV and CFD could be significant enough at this station to cause such a discrepancy. In contrast, the flow at W2 and W3 likely did not pass through the strongest adverse pressure gradient region at the windward foot of the hill and has experienced a milder pressure gradient history. The flow at W2 and W3 is thus likely less likely to exhibit discrepancies between the CFD and the real-world flow, as the upstream flow history and pressure gradients it has experienced are much milder than other regions over the bump surface.
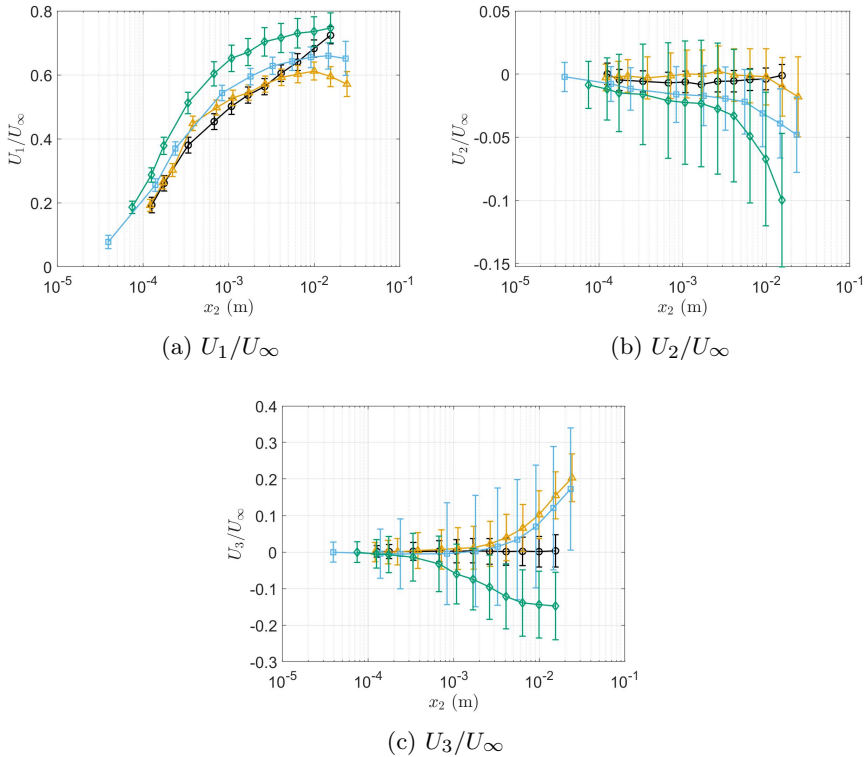
(a) U_1/U_∞

(b) U_2/U_∞

(c) U_3/U_∞

Fig. 9: Components of the mean velocity in local wall-shear stress coordinates, normalized by the freestream velocity. Symbols as in Table 2.

3.2 Mean Velocities and Turbulence

LDV measurements were collected in global tunnel coordinates, as shown in Fig. 2, and transformed into local wall-shear stress coordinates for analysis. In this coordinate system, the x_1-axis points in the estimated direction of the wall-shear stress vector at the wall via the mean flow angle closest to the surface, indicated in Fig. 7b by black arrows. The x_2-axis is perpendicular to the local surface tangent plane, and the x_3-axis completes a right-handed coordinate system.

As shown in Fig. 9, the flow begins largely 2D with near-zero components in U_2 and U_3 at W1. However, the flow experiences vastly different physics in different regions over the BeVERLI Hill, with varying levels of skewing and streamwise acceleration depending on the location on the model, as discussed. Though the U_2 and U_3 components are near-zero near the wall due to the wall-shear stress coordinate system, the U_3 components for all stations on the bump increase significantly further away from the surface due to the flow skewing. The U_2 components are near-zero for all profiles, although all profiles

(a) $\overline{u_1'^2}/U_\infty^2$

(b) $\overline{u_2'^2}/U_\infty^2$

(c) $\overline{u_3'^2}/U_\infty^2$

(d) $\overline{u_1'u_2'}/U_\infty^2$

(e) $\overline{u_2'u_3'}/U_\infty^2$

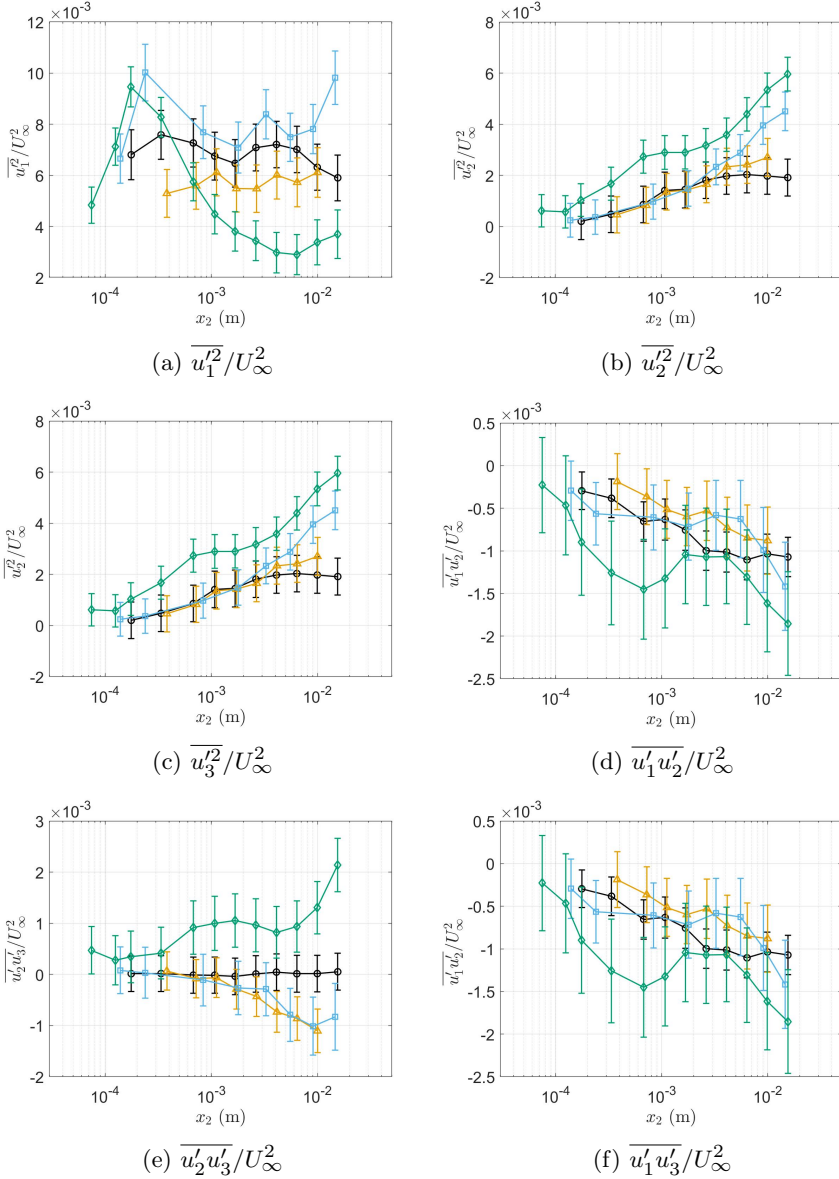(f) $\overline{u_1'u_3'}/U_\infty^2$

Fig. 10: Components of the Reynolds stress in local shear-stress coordinates, normalized by the freestream velocity. Symbols as in Table 2.

on the hill experience a small, increasingly negative component of U_2 as a function of height above the surface, especially at Station W5. This is an artifact of the strong tilt of the local surface normal (53° relative to the X_1-axis) wall-normal coordinate rotation. Near the wall, the flow flow is nearly
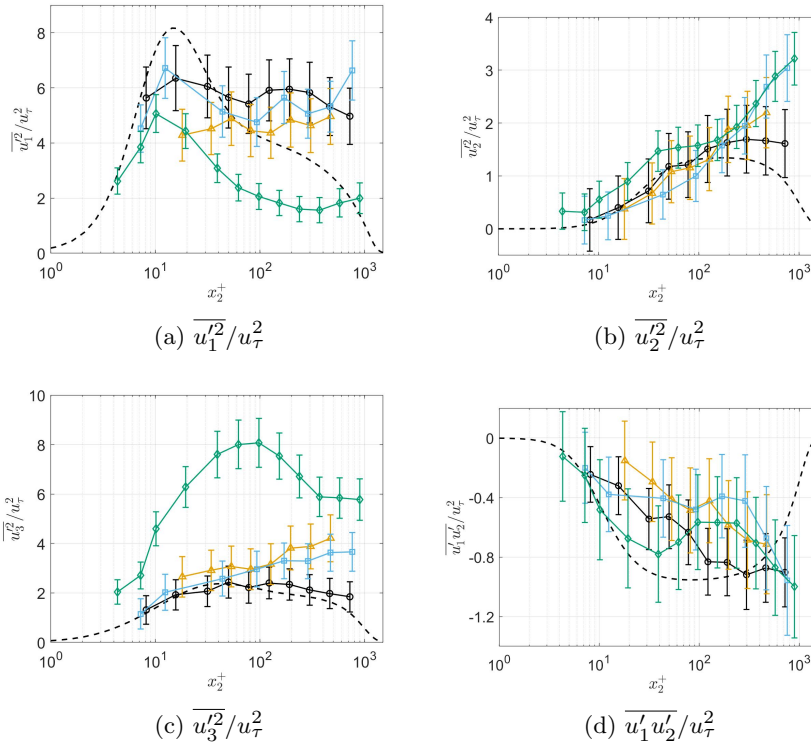
Fig. 11: Selected Reynolds stresses in wall-shear stress coordinates, normalized by u_τ and compared to the 2D equilibrium DNS data to the DNS data of Schlatter and Örlü (2010). Symbols as in Table 2.

tangential to the surface. Further above the wall, the body of the hill acts as a constriction, accelerating the flow and compressing the streamlines together to squeeze past the body. In the wall-normal coordinate system, this appears as a $-U_2$ component, as the streamlines passing through this profile are accelerated strongly in the outer region and squeezed together. This results in streamlines that are no longer parallel to the local surface curvature and appear to have a negative wall-normal velocity component.

The behavior in the Reynolds stresses in Figs. 10 and 11 is even more varied between stations than the mean velocities. Select Reynolds stress components are shown in Fig. 11 normalized on the friction velocity for comparison with equilibrium 2D TBL behavior. The $\overline{u_1' u_3'}/U_\infty^2$ and $\overline{u_2' u_3'}/U_\infty^2$ stresses are approximately zero within uncertainties at W1. The enhanced outer peak in $\overline{u_1'^2}/U_\infty^2$ is also consistent with an adverse pressure gradient turbulent boundary layer, like that of Harun et al (2013). The shear stress $\overline{u_1' u_2'}/u_\tau^2$ appears to be reduced compared to the 2D ZPG case, unlike the typical increase in Reynolds shear stress that would be expected in an APG TBL, as seen when compared

to the zero-pressure gradient (ZPG) direct numerical simulation (DNS) data of Schlatter and Örlü (2010) in Fig. 11.

In contrast, all three stations on the bump have significant components of both normal and shear stresses. Stations W2 and W3, located near each other and in a region of similar pressure gradient and pressure gradient histories, experience very similar turbulence behavior, as well as significant skewing of the near-wall flow relative to the tunnel X_1-axis and local concave curvature (see Fig. 6). While concave curvature generally has a destabilizing effect on a 2D TBL, Baskaran et al (1990) found that the combined effects of mild convex and concave curvature and mean flow three-dimensionality were small compared to the impact of curvature and three-dimensionality when applied individually, so it is likely that the difference in local pressure gradient and the different pressure gradient history of the flow in this region is a larger influence. The behavior between the stations primarily differs in $\overline{u_1'^2}/U_\infty^2$. The inner-region peak in $\overline{u_1'^2}/U_\infty^2$ is not captured at station W2, and the behavior above the x_2^+ peak of $\overline{u_1'^2}$ is lower in magnitude than at nearby station W3.

Station W5 experiences very different turbulence behavior than the other stations due to the different flow history, pressure gradients, and local curvature in this region. Here, the flow most notably experiences a decrease in the peak of $\overline{u_1'^2}/U_\infty^2$, a sharp increase in the magnitude of $\overline{u_3'^2}/U_\infty^2$, and an inflection point in $\overline{u_1'u_2'}/U_\infty^2$ in the log layer. Insight into the significant difference between the turbulence at Station W5 and the other stations can be provided by analyzing the Reynolds stress production. The production tensor, $\mathcal{P}_{ij}$, is shown in Eq. 4 (Pope, 2000).

$$\mathcal{P}_{ij} \equiv -\overline{u_i'u_k'}\frac{\partial U_j}{\partial x_k} - \overline{u_j'u_k'}\frac{\partial U_i}{\partial x_k} \tag{4}$$

Due to the nature of the LDV measurements, only surface-normal gradients were captured. The production is thus approximated for the Reynolds stresses by assuming that only surface-normal mean velocity gradients are significant and neglecting mean velocity gradients in the x_1- and x_3-directions, as shown in Eq. 5.

$$\mathcal{P}_{22} \approx -2\overline{u_2'^2}\frac{\partial U_2}{\partial x_2} \tag{5a}$$

$$\mathcal{P}_{33} \approx -2\overline{u_2'u_3'}\frac{\partial U_3}{\partial x_2} \tag{5b}$$

$$\mathcal{P}_{12} \approx -\overline{u_2'^2}\frac{\partial U_1}{\partial x_2} \tag{5c}$$

$$\mathcal{P}_{23} \approx -\overline{u_2'^2}\frac{\partial U_3}{\partial x_2} - \overline{u_2'u_3'}\frac{\partial U_2}{\partial x_2} \tag{5d}$$

For all stations, the production of $\overline{u_1'u_2'}$ is dominated by the gradient of U_1, as this component is more than an order of magnitude larger than the velocity

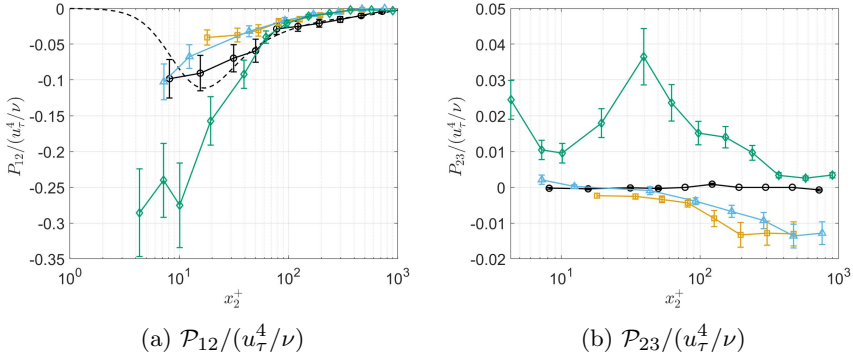(a) $\mathcal{P}_{12}/(u_\tau^4/\nu)$ (b) $\mathcal{P}_{23}/(u_\tau^4/\nu)$

Fig. 12: Reynolds shear stress production, estimated as in Eq. 5.

gradients in the other coordinate directions. The difference in shear stress between stations W2 and W3 and station W5 can be attributed to the larger $\overline{u_2'^2}$ component at W5 further enhancing production of $\overline{u_1'u_2'}$. The production throughout the profiles are shown in Fig. 12, and $\mathcal{P}_{12}$ is notably enhanced at W5 compared to stations W2 and W3.

The behavior between profiles begins to differ in the other stress components due to the significant $\partial U_2/\partial x_2$ parameter at W5, where $\partial U_2/\partial x_2$ is of the same order of magnitude as $\partial U_3/\partial x_2$. At W2 and W3, due to the smaller magnitude of $\partial U_2/\partial x_2$, the $-\overline{u_2'^2}\frac{\partial U_3}{\partial x_2}$ term dominates in the production of $\overline{u_2'u_3'}$. In contrast, at W5, the term containing $\partial U_2/\partial x_2$ is non-negligible, and thus contributes to a larger magnitude $\overline{u_2'u_3'}$ profile at W5 as the production is much more significant at this station, as shown in Fig. 12b. The significant $\partial U_3/\partial x_2$ and $\overline{u_2'u_3'}$ components together then contribute to enhance the production of $\overline{u_3'^2}/U_\infty^2$ at W5, resulting in a very large component of $\overline{u_3'^2}/U_\infty^2$ in comparison to the other stations.

3.3 Total Shear Stress

In the wall-shear stress coordinate system, the total shear stress is composed of the viscous component, $\mu\partial U_1/\partial x_2$, which is maximum in the viscous sublayer, and the turbulent component, $\rho(\overline{u_1'u_2'}^2 + \overline{u_2'u_3'}^2)^{1/2}$. The wall-parallel momentum equations can be simplified to focus upon the behavior of the flow in the limit of being in the viscous sublayer by ignoring the inertial terms and Reynolds shear stresses and assuming that the x_1-axis is in the wall-shear direction, resulting in Eqs. 6 and 7.

$$U_1^+ = \frac{\partial P^+}{\partial x_1^+}\frac{x_2^{+2}}{2} + x_2^+ \tag{6}$$

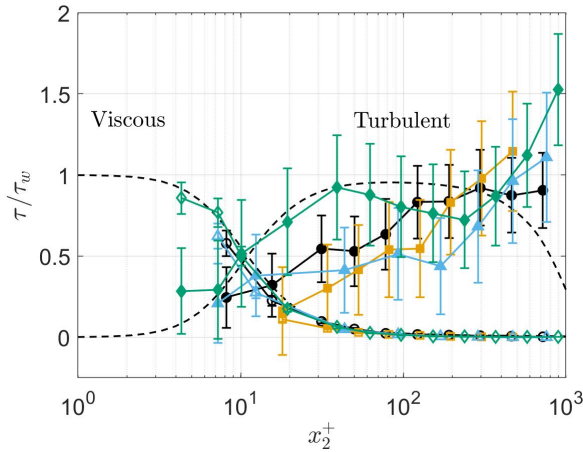$$U_3^+ = \frac{\partial P^+}{\partial x_3^+}\frac{x_2^{+2}}{2} \tag{7}$$

Fig. 13: Comparison of viscous and turbulent shear stress components at the four stations of interest, compared to the 2D DNS data of Schlatter and Örlü (2010) at $Re_\theta = 4060$. Symbols as in Table 2. Open symbols indicate viscous stress components, $\partial U_1^+/\partial x_2^+$, and filled symbols indicate turbulent shear stress components, $\sqrt{\overline{u_1'u_2'}^{+2} + \overline{u_2'u_3'}^{+2}}$.

In this wall-shear stress coordinate system, an FPG in the x_1-direction indicates that the flow is being accelerated in the wall-shear direction. Skewing is caused by a lateral pressure gradient perpendicular to the local wall-shear direction, inducing a non-zero U_3^+ component. If the pressure gradient is assumed to be approximately constant as a function of height in the viscous sublayer, then an FPG in the wall-shear direction will cause the viscous stress to reduce more rapidly from the wall in wall units than a ZPG or APG due to the influence of the pressure term.

The turbulent shear stress is also very sensitive to flow conditions. The presence of mean streamwise vorticity is known to impact the quasi-coherent turbulent structures that are responsible for the production of $\overline{u_1'u_2'}$ and $\overline{u_2'u_3'}$ Johnston and Flack (1996) and lead to the reduction of these shear stress components. However, Flack and Johnston (1998) have also found that $\tau_{turbulent}$ increases outside of the buffer layer in regions of increasing three-dimensionality. This can also be seen at some stations in the data of Ölçmen et al (2001). For both experiments, although $\overline{u_1'u_2'}/u_\tau^2$ decreased in magnitude as the three-dimensionality of the flow increased, an increase in the magnitude of $\overline{u_2'u_3'}/u_\tau^2$ compensated for this behavior and led to an increase in $\tau_{turbulent}$ outside of the buffer layer.

The viscous and turbulent shear stress components of the total shear stress in the BeVERLI Hill stations of interest are normalized by τ_w, computed via u_τ, in Fig. 13 and compared with the 2D ZPG equilibrium boundary layer DNS of Schlatter and Örlü (2010). As shown in Fig. 13, stations W2 and W3

both experience a region below $x_2^+ \approx 200$ where the turbulent shear stress is significantly reduced and not able to balance out the viscous stress it drops outside of the linear sublayer. This results in a total stress distribution that is far from the equilibrium $0.95 \leq \tau/\tau_w \leq 1$ that is typically present in 2D ZPG boundary layers and is assumed in some LES equilibrium-stress models, such as those of Piomelli et al (1989) and Marusic et al (2001).

Above $x_2^+ \approx 200$, there is a sharp increase in the turbulent stress, as was also observed by Flack and Johnston (1998) (though in their case, this was observed above $x_2^+ \approx 50$). There is, therefore, a region below $x_2^+ \approx 200$ that is dominated by viscous and wall-effects, and a region above this point of the boundary layer where the effects of the crossflow stress $\overline{u_2' u_3'}$ begin to contribute more significantly as the flow turns away from the local wall-shear stress direction. At Stations W2 and W3, this significant drop in turbulent shear stress is expected, as a reduction in turbulent shear stress is often seen in 3D flows, such as the experimental flow of Bradshaw and Pontikos (1985) and the DNS simulations of Moin et al (1990), where the significant near-wall skewing and transverse strain suppresses the pressure-strain term in the turbulent transport.

In contrast, at station W5, the flow behavior is quite different due to the different pressure gradient and flow history in this region. Notably, there is a small region near the wall where the turbulent shear stress approximately matches the 2D equilibrium DNS profile. This continues until the edge of the buffer layer, after which the shear stresses decrease for a portion of the log layer before sharply increasing again, similar to stations W2 and W3. Throughout the profile, $\overline{u_2'^2}/u_\tau^2$ is notably elevated compared to the 2D equilibrium case, despite the approximately equilibrium behavior in $\overline{u_1' u_2'}/u_\tau^2$ below the buffer layer, which suggests that the flow has not reverted to an approximately two-dimensional state in the near-wall region and is still three-dimensional. The elevated $\overline{u_2'^2}/u_\tau^2$ and $\overline{u_1' u_2'}/u_\tau^2$ profiles relative to stations W2 and W3 is consistent with what would be expected from analysis of the production of each turbulence component, as the production of $\mathcal{P}_{12}$ and $\mathcal{P}_{22}$ are linked through the $\overline{u_2'^2}$ component. The turbulent shear stress component in this region is dominated by the contribution from $\overline{u_1' u_2'}$, which suggests that the same mechanisms that led to a more equilibrium $\overline{u_1' u_2'}/u_\tau^2$ distribution in the buffer layer (Fig. 11d) are contributing to the more equilibrium turbulent shear stress behavior.

The profiles are compared in Fig. 15 with the 3D TBL on a flat wall around a wing-body junction from Ölçmen et al (2001) in regions that experience similar pressure gradient and skewing behavior but without wall curvature. A schematic of the local freestream and wall-shear stress directions in their experiment is shown in Fig. 14. As shown, the flow experiences increasing skewing as the near-wall flow feels the impact of the airfoil presence more strongly than the freestream flow. After Station O3, the magnitude of the skewing relative to the freestream flow begins to decrease, as the wall-shear stress and freestream flow directions become nearly identical. Of the nine flow stations, four are of particular interest for comparison to the skewed flow on the BeVERLI Hill.
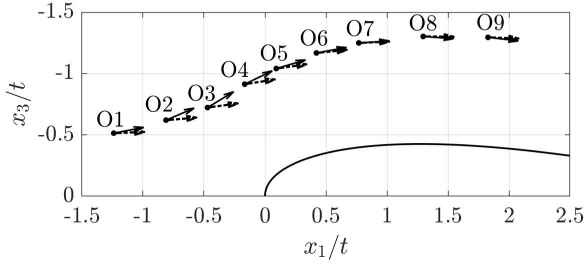
967
968
969
970
971
972
973
974
975
976

Fig. 14: Top-down view of the profile locations of the 3D flow on a flat wall around a wing-body junction, with the x_2-coordinate normal to the page. Solid arrows indicate local wall-shear stress direction, while dashed arrows indicate local freestream flow direction. Adapted from Ölçmen et al (2001).

981
982
983
984
985
986
987
988
989
990
991
992
993
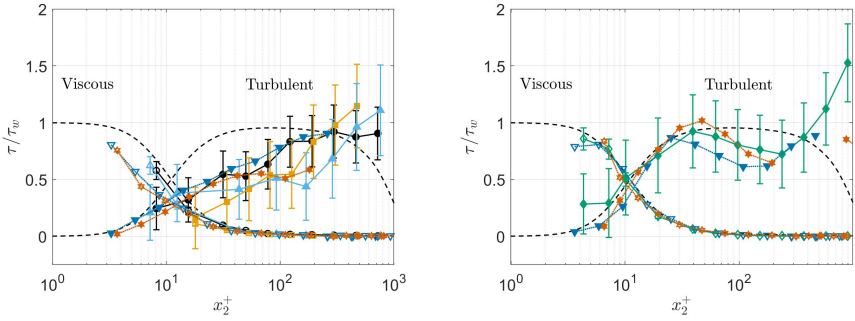
(a) BeVERLI symbols as in Table 2, ▽: Station O3; ✡: Station O4.

(b) BeVERLI symbols as in Table 2, ▽: Station O6; ✡: Station O7.

Fig. 15: Comparison of turbulent and viscous shear stress behavior of selected stations on the BeVERLI Hill with the 2D equilibrium DNS data of Schlatter and Örlü (2010) and the 3D flat-wall TBL of Ölçmen et al (2001). (a) Stations W1, W2, and W3 of the BeVERLI Hill compared with stations O3 and O4 of Ölçmen et al (2001). (b) Station W5 of the BeVERLI Hill compared with stations O6 and O7 of Ölçmen et al (2001).

1002
1003

At Stations O3 and O4 of Ölçmen *et al.*, the flow is extremely skewed ($> 30°$ from the upstream flow direction), and streamwise pressure gradient is favorable as it passes around the side of the wing-body junction. This global flowfield behavior is similar to that of stations W2 and W3 of the BeVERLI flow, and, as shown, results in similar turbulent shear stress behavior, as shown in Fig. 15a. However, the data of Ölçmen *et al.* is missing in the region in which Stations W2 and W3 begin experiencing a sharp increasing in the turbulent

shear stress, so it is not possible to identify if this behavior is also present in the juncture flow.

A similar trend follows for Ölçmen *et al.*'s stations O6 and O7 and the hill's station W5, as seen in Fig. 15b. At both stations, the flow is much less skewed than at previous stations as it recovers past the junction and is also experiencing a stronger streamwise FPG than further upstream in the flow, similar to W5. Notably, all three stations experience a region through the buffer layer where the turbulent shear stress nearly matches the 2D DNS, before all show a sudden drop in turbulent shear stress above the buffer layer, and a subsequent increase above $x_2^+ \approx 200$. Because this behavior is present in both the flat wall and hill flows, this suggests that the mechanisms driving this return to an equilibrium shear stress distribution in below the buffer layer is driven by pressure gradients and pressure gradient histories rather than dominated by curvature effects. However, curvature effects have not been quantified and remain the subject of future work.

4 Conclusion

LDV measurements of the flow upstream of and on the three-dimensional BeVERLI Hill model were used to analyze the fluid physics at those stations. As shown, the selected stations experience significantly different mean flow and turbulence behavior due to differing pressure gradients, radii of curvature, and history effects at each station. Of these effects, local pressure gradient and skewing appear to be the strongest influences on the turbulence at each station. Curvature effects due to the 3D hill geometry were not specifically examined in this study and will instead be a focus of future work.

Analysis of the BeVERLI Hill data and comparison with the 3D TBL on a flat wall around a wing-body junction from Ölçmen et al (2001) show there is no region in the flow over the BeVERLI Hill where equilibrium assumptions regarding the shear stress distribution are valid. This is especially severe in strongly skewed flow, such as at stations W2 and W3. In accelerated regions of the flow with milder flow skewing, such as at station W5, the turbulent stresses below the buffer layer may approximately follow an equilibrium distribution, before diverging significantly from this behavior above $x_2^+ \approx 30$. Similar behavior seen in the BeVERLI Hill flow was also observed in the flat wall flow around a wing-body juncture of Ölçmen et al (2001) in regions with similar skewing and pressure gradient behavior. Turbulence models that rely on this equilibrium shear stress assumption will not be able to accurately predict the turbulence behavior of 3D flow.

Declarations

Ethics approval and consent to participate

Not applicable.

Consent for publication

Not applicable.

Availability of data and materials

Data used in this work will be made publicly available this fall through NASA.

Competing interests

The authors have no relevant financial or non-financial interests to disclose.

Funding

Authors' Contributions

All authors contributed to the study conception and design. Material preparation, data collection, and analysis of pressure and LDV data were performed by J.D., with assistance from A.B. and A.G in pressure data collection. Material preparation, data collection, and analysis of oil flow visualization images were performed by J.D. and A.G. Simulations were performed by A.G. The first draft of the manuscript was written by J.D. and all authors commented on previous versions of the manuscript. All authors read and approved the final manuscript.

Acknowledgments

References

Aeschliman DP, Oberkampf WL (1998) Experimental Methodology for Computational Fluid Dynamics Code Validation. AIAA Journal 36(5):733–741. https://doi.org/10.2514/2.461

Anderson SD, Eaton JK (1989) Reynolds stress development in pressure-driven three-dimensional turbulent boundary layers. Journal of Fluid Mechanics 202:263–294. https://doi.org/10.1017/S0022112089001187

Baskaran V, Pontikis YG, Bradshaw P (1990) Experimental investigation of three-dimensional turbulent boundary layers on 'infinite' swept wings. J Fluid Mech 211:95–122. https://doi.org/10.1017/S0022112090001513, URL https://doi.org/10.1017/S0022112090001513

Bell JH, Heineck JT, Zilliac G, et al (2012) Surface and flow field measurements on the FAITH hill model. In: 50th AIAA Aerospace Sciences Meeting. American Institute of Aeronautics and Astronautics, Nashville, TN, pp 2012–0704, https://doi.org/10.2514/6.2012-704, URL http://dx.doi.org/10.2514/6.2012-704

Bose ST, Park GI (2018) Wall-Modeled Large-Eddy Simulation for Complex Turbulent Flows. Annual Review of Fluid Mechanics 50:535–561. https://doi.org/10.1146/annurev-fluid-122316-045241

Bradshaw P, Pontikos NS (1985) Measurements in the turbulent boundary layer on an 'infinite' swept wing. Journal of Fluid Mechanics 159:105–130. https://doi.org/10.1017/S0022112085003123

Byun G, Simpson RL (2006) Structure of Three-Dimensional Separated Flow on an Axisymmetric Bump. AIAA Journal 44(5):999–1008. https://doi.org/10.2514/1.17002, URL http://arc.aiaa.org

Devenport WJ, Lowe KT (2022) Equilibrium and non-equilibrium turbulent boundary layers. Progress in Aerospace Sciences 131(100807):1–50. https://doi.org/10.1016/j.paerosci.2022.100807, URL https://linkinghub.elsevier.com/retrieve/pii/S0376042122000033

Duetsch-Patel JE, Vishwanathan V, Minionis JB, et al (2020) Aerodynamic Design and Assessment of Modular Test Section Walls for CFD Validation in Hybrid Anechoic Wind Tunnels. In: AIAA SciTech 2020 Forum, Orlando, pp 2020–2214, https://doi.org/10.2514/6.2020-2214

Flack KA, Johnston JP (1998) Near-wall flow in a three-dimensional boundary layer on the endwall of a 30° bend. Experiments in Fluids 24:175–184. https://doi.org/10.1007/s003480050164

Gargiulo A, Vishwanathan V, Fritsch DJ, et al (2020) Examination of Flow Sensitivities in Turbulence Model Validation Experiments. In: AIAA SciTech 2020 Forum, Orlando, pp 2020–1583, https://doi.org/10.2514/6.2020-1583

Harun Z, Monty JP, Mathis R, et al (2013) Pressure gradient effects on the large-scale structure of turbulent boundary layers. Journal of Fluid Mechanics 715:477–498. https://doi.org/10.1017/jfm.2012.531

Johnston JP, Flack KA (1996) Review - Advances in Three-Dimensional Turbulent Boundary Layers With Emphasis on the Wall-Layer Regions. Journal of Fluids Engineering 118:219–232. https://doi.org/10.1115/1.2817367

Marusic I, Kunkel GJ, Porté-Agel F (2001) Experimental study of wall boundary conditions for large-eddy simulation. Journal of Fluid Mechanics 446:309–320. https://doi.org/10.1017/s0022112001005924

Moin P, Shih TH, Driver D, et al (1990) Direct numerical simulation of a three-dimensional turbulent boundary layer. Physics of Fluids 2(10):1846–1853. https://doi.org/10.1063/1.857658

Ölçmen SM, Simpson RL, George J (2001) Some Reynolds number effects on two-and three-dimensional turbulent boundary layers. Experiments in Fluids 31:219–228. URL http://www.aoe.vt.edu/

Piomelli U, Ferziger J, Moin P, et al (1989) New approximate boundary conditions for large eddy simulations of wall-bounded flows. Physics of Fluids A 1(6):1061–1068. https://doi.org/10.1063/1.857397

Pope SB (2000) Turbulent Flows. Cambridge University Press, Cambridge

Rhode MN, Oberkampf WL (2017) Estimation of Uncertainties for a Model Validation Experiment in a Wind Tunnel. Journal of Spacecraft and Rockets 54(1):155–168. https://doi.org/10.2514/1.A33563

Schlatter P, Örlü R (2010) Assessment of direct numerical simulation data of turbulent boundary layers. Journal of Fluid Mechanics 659:116–126. https://doi.org/10.1017/S0022112010003113

Smith BL, Oberkampf WL (2014) Limitations of and Alternatives to Traditional Uncertainty Quantification for Measurements. In: ASME 2014 4th Joint US-European Fluids Engineering Division Summer Meeting. ASME, Chicago, IL, pp 1–12

Vishwanathan V, Szoke M, Duetsch-Patel JE, et al (2020) Aerodynamic Design and Validation of a Contraction Profile for Flow Field Improvement and Uncertainty Quantification in a Subsonic Wind Tunnel. In: AIAA SciTech 2020 Forum, Orlando, pp 2020–2211, https://doi.org/10.2514/6.2020-2211